Reviews of Electromagnetics, Vol. IV, 2025
EuCAP 2025 Special Issue
DOI: 10.53792/RoE/2025/25013

Reviews of Electromagnetics
EuCAP 2025 Special Issue

Angle-Resolved Channel Measurements at 28 and 160 GHz in Open Office Environment

Mathis Schmieder[1]*, Alper Schultze[1], Niclas Kullig[1], Ramez Askar[1], Michael Peter[1], Wilhelm Keusgen[2]

Abstract
This paper presents channel measurements and modeling at 28 and 160 GHz in an industrial-style open office environment with angular information at the receiver. Channel impulse response snapshots are captured at 135 measurement positions for both frequencies and are evaluated in terms of power metrics, delay, and angular characteristics. Frequency-dependent models for path loss, delay, and angular spread of arrival and K-factor are estimated, and large-scale parameter cross-correlations are evaluated. The measurements are compared to the 3GPP TR 38.901 channel model in the Indoor-Office and Indoor-Factory scenario. Results show that delay and angle spread are not frequency dependent in this environment although twice as many multi-path components were identified at 28 GHz compared to 160 GHz.

Key terms
mm-wave channel sounding, sub-THz, 6G, channel measurements, channel modeling, propagation, open office environment, industrial environment

[1] *Fraunhofer Institute for Telecommunications, Heinrich Hertz Institute, HHI, Berlin, Germany*
[2] *Technische Universität Berlin, Germany*
***Corresponding author**: mathis.schmieder@hhi.fraunhofer.de

Received: 23/05/2025, Accepted: 04/11/2025, Published: 04/12/2025

1. Introduction

The evolution of wireless communication networks into their sixth and subsequent generations entails a significant expansion into the sub-terahertz (sub-THz) frequency spectrum, driven by the escalating demand for higher data rates [1, 2]. The preceding fifth-generation (5G) networks similarly advanced, incorporating centimeter-wave (cmW) frequency bands ranging from 24.25 GHz to 29.5 GHz—labeled as band n257 and band n258 according to 3rd Generation Partnership Project (3GPP) terms [3]. Prior to the deployment of these advancements, it is imperative to investigate the propagation characteristics of the sub-THz bands through rigorous channel measurement (sounding) and parameter extraction processes. This foundational work is essential for the development of a representative channel model. In this study, we present channel measurements and analyses conducted at 28 GHz and 160 GHz carrier frequencies within an identical environment and operational setting, and compare the results to the 3GPP technical report (TR) 38.901 [4] channel model. The comparative analysis of the extracted parameters from these two frequency bands – one in the cmW range and the other in the sub-THz range – measurements provides fair metrics and assessment factors for potential future sixth-generation (6G) and beyond deployments. In other words, the comparison evaluates the feasibility of using the sub-THz band in existing cmW infrastructure locations, such as basestations. Notably, utilizing these established sites for deployment significantly contributes to reducing both capital expenditures (CAPEX) and operation expenditures (OPEX) in the evolving mobile network.

1.1. State of the Art

Numerous state-of-the-art articles presented industrial channel measurement in the cmW and millimeter wave (mmW) frequency ranges. In contrast, a few published articles discussed indoor factory/industrial channel measurements and models in the sub-THz frequency range. Table 1 summarizes the key parameters of these articles. As indicated in the table, the carrier frequencies range from 132 GHz to 304.2 GHz with bandwidth up to 8 GHz utilizing a time-domain sounding approach, and up to 10 GHz using a vector network analyzer (VNA) as a frequency-sweeping approach.

Table 1: Sub-THz state-of-the-art channel measurement comparison

Work	Year	Carrier frequency	Bandwidth	Sounder principle	Compared cmW/mmW/sub-THz bands
This	2025	160 GHz	1 GHz	TD[a], FZC[b] sequence	28 GHz
[5]	2025	160 GHz	1 GHz	TD[a], FZC[b] sequence	28 GHz
[6]	2023	142 GHz	4 GHz	TD[a], Sliding correlation	none
[7]	2024	142 GHz	4 GHz	TD[a], Sliding correlation	28 GHz, 30 GHz, 60 GHz and 108 GHz
[8]	2024	132 GHz	5.5 GHz	VNA[c]	28 GHz and 38 GHz
[9]	2024	140 GHz	4 GHz	VNA[c]	28 GHz
[10]	2024	220 GHz	10 GHz	VNA[c]	108 GHz and 142 GHz
[11]	2024	304.2 GHz	8 GHz	TD[a], m-sequence	none
[12]	2022	300 GHz	2 GHz	TD[a], FZC[b] sequence	none
[13]	2024	160 GHz	2 GHz	TD[a], FZC[b] sequence	none
[14]	2023	303.8 GHz	5 GHz	TD[a], 12bit m-sequence	none
[15]	2023	300 GHz	2 GHz	TD[a], FZC[b] sequence	none
		304.2 GHz	8 GHz	TD[a], m-sequence	
[16]	2025	165 GHz	1.2 GHz	TD[a], Sliding correlation	none
[17]	2025	300 GHz	8 GHz	TD[a], Multitone signal	none
[18]	2023	300 GHz	8 GHz	TD[a], Multitone signal	60 GHz
[19]	2024	158 GHz / 300 GHz	2 GHz	TD[a], FZC[b] sequence	none
[20]	2024	145 GHz	18 GHz	Digital frequency sweep, DDFS[d]	86 GHz

[a] Time domain
[b] Frank Zadoff Chu
[c] Vector network analyzer
[d] Direct digital frequency synthesizer

A study similar to this work was published in [9], where indoor propagation channel measurements at 28 GHz and 140 GHz in an entrance hall are compared to each other and to the 3GPP TR 38.901 [4] model. It was found that the 3GPP ABG path loss (PL) model aligns well with measured line of sight (LOS) PL, but pporly fits non-line-of-sight (NLOS). Compared to the existing model, the measured angular spread (AS) is lower and shows little frequency dependence, whereas the delay spread (DS) decreases with frequency and differs from the model values. It was furthermore found that the power angular profile (PAP) shapes are similar at 28 GHz and 140 GHz.

1.2. Organization

This paper is an extended version of the original work presented in [5]. Novelties include the addition of an evaluation of power delay and angular profiles, and a comparison between the profiles at the two frequencies. It was furthermore evaluated if the 3GPP TR 38.901 [4] channel model in either Indoor-Hotspot (InH) or Indoor-Factory (InF) scenario is a fitting representation for the measurement results. A potential distance dependency was assessed for both root mean square (RMS) DS and azimuth spread of arrival (ASA). Finally, the large scale parameter (LSP) cross-correlations were calculated separately for both frequencies used as a measure for the similarity of the radio channel between the two frequencies.

The rest of the paper is organized as follows: Section 2 introduces the channel sounder setup. Section 3 describes the measurement scenario and the conducted procedure of the channel measurements. Section 4 provides a brief review of the relevant 3GPP channel models. Then, Section 5 presents a detailed evaluation of the channel measurement results. Finally, Section 6 concludes the article.

2. Channel Sounder Setup

In the following section, the channel sounder setup used to conduct the measurements is described. Fig. 1 shows a simplified block diagram of the setup, which follows the principle of correlative time-domain channel sounding and uses both commercial off-the-shelf test & measurement equipment, and specific components developed at Fraunhofer HHI.

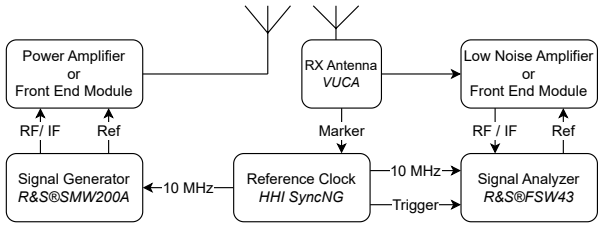

Figure 1: Block diagram of the channel sounder setup.

At the transmitter (TX), a vector signal generator (VSG) (*R&S® SMW200A*) is used to generate the sounding signal with a bandwidth of up to 2 GHz directly at the radio frequency (RF) of 28 GHz, or at an intermediate frequency (IF) for the measurements at 160 GHz. Here, an additional front end module (FE) (*R&S® FE170ST*) is used to up-convert the signal to the RF. Power amplifiers are used to bring the signal level to a total power of 33 dBm at 28 GHz (*RF-Lambda RP18G40GSPA2*), and 10 dBm at 160 GHz (*Fraunhofer IAF M286AMPG*). Finally, the sounding signal is transmitted using vertically polarized omnidirectional antennas. At 28 GHz, a custom wide-band bi-conical antenna was used that is resonant from 24 GHz to 67 GHz. For 160 GHz, a commercial antenna usable over the whole D-band (*Eravant SAO-1141740330-06-S1*) was available.

On the receiver side, the signal is captured using virtual uniform circular arrays (VUCAs) [21] with similar omnidirectional antenna elements, allowing near-instantaneous angle-resolved measurements. During one revolution of the antenna, 1000 sequences of the periodic sounding signal are captured. Assuming that the radio channel was static for the duration of one revolution, a virtual circular array antenna with 1000 elements is constructed, and spatial information about the received signal can be estimated. Fig. 2 shows the D-band VUCA together with the FE on a tripod looking towards the TX. The D-band VUCA is built around two two TE_{10}-to-TE_{01} mode transducers that form a waveguide rotary joint. As the electrical field of the TE_{01} mode is circular and invariant to change of rotation angle, and vanishes on the walls of the waveguide, this mode enables the construction of efficient rotary joints with low insertion losses. Because the structure of a TE_{10}-to-TE_{01} mode transducer like the one described in [22] is not feasible to manufacture in a conventional subtractive way, the parts for the design used in this publication were 3D-printed by means of selective laser sintering (SLS) in AL6061 aluminium. Initial evaluation of the insertion loss of the VUCA including two transducers reveals that it does not exceed −5 dB over the usable frequency range from 145 GHz to 170 GHz.

Figure 2: D-Band VUCA looking towards the TX.

After reception by the VUCA, the signal is amplified by a low noise amplifier (LNA) (*Mini-Circuits ZVA-24443G1+* with a gain of 45 dB at 28 GHz, and *AT Microwave AT-LNA-110170-3306E* with a gain of 33 dB at 160 GHz) and sampled using a vector signal analyzer (VSA) *R&S® FSW43*. At 160 GHz, a FE (*R&S® FE170SR*) is used to down-convert the RF to IF before sampling. A distributed clock and trigger generator (*Fraunhofer HHI SyncNG*) provides a shared 10 MHz reference clock to all measurement devices and also enables the coherent triggering of the receiver (RX).

Table 2: Channel sounder parameters

Parameter	Value and unit	
System parameters		
Carrier frequency	28 GHz	160 GHz
Sounding bandwidth	2 GHz	1 GHz
Sampling rate at Tx	2.4 GHz	1.2 GHz
Sampling rate at Rx	2.5 GHz	1.25 GHz
Maximum measurable PL	188 dB	142 dB
Evaluation threshold	20 dB	
Front end parameters		
Transmit power ($P_{1\mathrm{dB}}$)	33 dBm	10 dBm
LNA Gain	45 dB	33 dB
Antenna parameters		
Omnidirectional antenna gain	0 dBi	3 dBi
Vertical 3-dB beamwidth	120°	30°
Sequence duration	50 µs	300 µs
Rotational speed	1200 RPM	200 RPM
Diameter of VUCA	97.8 mm	
Number of virtual elements	1000	
Distance between virtual elements	0.307 mm	
Sequence parameters		
Sequence duration	50 µs	300 µs
Sequence length in samples	100.000	300.000
Correlation gain	50 dB	54.8 dB

As sounding signal, a complex, periodic Frank-Zadoff-Chu (FZC) sequence [23] is used for its optimal correlation characteristics. At 28 GHz, the sequence has 100.000 samples with a bandwidth of 2 GHz, corresponding to a duration of 50 µs. In order to capture 1000 sequences over one revolution of the antenna, the rotational speed has to be set to 1200 revolutions per minute (RPM). Due to the higher mass of the element of the 160 GHz, the rotational speed has to be limited to 200 RPM, which corresponds to a sequence duration of 300 µs. The bandwidth is reduced to 1 GHz to keep the time manageable that it takes to acquire, store, and download the measurement data, leading to a sequence length of 300.000 samples. A N-element FZC sequence achieves a correlation gain according to (1)

$$G_{\mathrm{corr|dB}} = 10\log_{10}(N_{\mathrm{seq}}), \tag{1}$$

resulting in a gain of 50 dB at 28 GHz and 54.8 dB at 160 GHz. Table 2 lists the important channel sounder parameters. The maximum measurable PL is defined as the difference between the transmit power and the noise floor which is evaluated in subsection 5.1.

3. Measurement Scenario and Procedure

The measurements were performed within the Fraunhofer HHI showroom in Berlin, Germany. This indoor location features an approximate floor space of 30 m × 15 m and a height of 4.25 m. It features high concrete-covered ceilings that are lined with large metal panels and is completely surrounded by glass windows that reach from floor to ceiling. Ten concrete pillars support the ceiling of the room. Floor tanks are distributed equidistantly throughout the whole area and are used as reference locations for the RX and TX positions. While the showroom mainly serves as an open office space for conferences and demo purposes, it also resembles an industrial-like environment due to the reflective metal-coated glass fronts, metal panels, and concrete features. Fig. 3 shows an overview of the measurement environment. As reflective clutter, several meeting tables with chairs were set up throughout the room, and TVs stood in front of the south wall and some pillars.

Figure 3: Overview of the measurement environment.

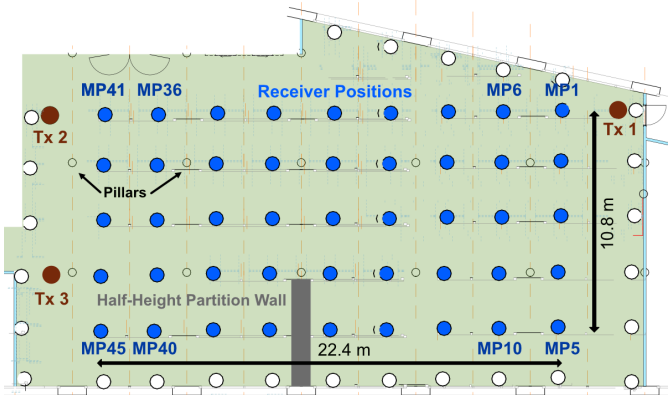

Figure 4: Floor plan of the measurement scenario, including TX and RX positions.

In most of the measurement position (MP), the showroom features a clear LOS between TX and RX, with only weak blockage due to the concrete pillars. To introduce some NLOS MP, one TX position (Tx3) was placed in line with the concrete pillars, shadowing it from some of the MP. Furthermore, a set of three TV walls was used to construct a half-height partition wall, as indicated in gray in Fig. 4 and also shown in Fig. 3. These walls are constructed of thin metal and measure 2.5 m in height, 1.4 m in width, and 0.3 m in depth each. In the end, 85 of the 135 measurements were in LOS condition, and 50 in NLOS.

A grid of 9×5 MPs was defined on the showroom floor plan, as shown in Fig. 4. These MP coincide with the floor tanks are spaced equidistantly, and are visualized as deep blue dots in Fig. 4. Besides the 45 RX positions, three TX positions were also defined and are shown as red dots in Fig. 4. Both TX and RX were set up at a height of 1.9 m above ground, which is the lowest height the mobile RX setup supports. As the TX antenna height mainly influences shadowing and the LOS probability, and an increased height would have led to even fewer MPs in NLOS condition, the TX height was chosen to be equal to the RX height. The minimum 3-dimensional (3D) distance between TX and RX was 3 m and the maximum was 27.6 m. The TX was placed fixed at the three TX positions, and the RX was set up on top of a wheeled dolly for easy relocation to each of the 45 MP. Overall, 135 measurements were conducted for each frequency.

4. 3GPP TR 38.901 Channel Model

Two indoor scenarios are defined by the 3GPP in their TR 38.901 channel model [4]: First is the Indoor-Office or Indoor-Hotspot (InH) scenario, which is valid for room sizes up to 120 m × 50 m × 3 m with inter-site distances of 20 m. The base station shall be mounted on the ceiling at a height of 3 m, and the user terminals are defined at a height of 1 m. The second is the industrial InF scenario, which is separated into several sub-scenarios for varying levels of density of "clutter". For the presented environment, the InF-SL (sparse clutter, low BS) model seems most appropriate: It is defined for rooms with a floor size of 20 m^2 to 160 000 m^2 and a ceiling height of 5 m to 15 m. The external walls and ceilings are defined to be concrete or metal, or metal-coated windows. Up to 40 % of the surface area is occupied by clutter, and the height of the BS antenna is at or below the average height of clutter. With a floor size of approximately 450 m^2, the measurement scenario falls within the limits of both model scenarios. The ceiling height of 4.25 m is above the upper limit of the InH scenario, but slightly lower than InF. Both ceilings and walls are concrete, metal-coated glass, or metal, as specified in the InF scenario. Although no lower bound for clutter percentage is specified in the InF model, the measurement scenario is certainly less packed than a typical industrial environment. In place of industrial machinery, TVs and meeting tables with chairs are set up throughout the room. None of the two indoor scenarios defined in 3GPP TR 38.901 is a perfect match to the measurement environment, but each can be applied to a certain degree.

$$PL_{\text{InH-LOS}} = 32.4 + 17.3\log_{10}(d_{3D}) + 20\log_{10}(f_c), \quad \sigma = 3, \tag{2a}$$
$$PL'_{\text{InH-NLOS}} = 17.30 + 38.3\log_{10}(d_{3D}) + 24.9\log_{10}(f_c), \quad \sigma = 8.29\,. \tag{2b}$$

$$PL_{\text{InF-LOS}} = 31.84 + 21.50\log_{10}(d_{3D}) + 19\log_{10}(f_c), \quad \sigma = 4, \tag{3a}$$
$$PL'_{\text{InF-NLOS}} = 33 + 25.5\log_{10}(d_{3D}) + 20\log_{10}(f_c), \quad \sigma = 5.7\,. \tag{3b}$$

For both scenarios, the channel model features a frequency-dependent path loss model according to equations (2) and (3).

Table 3: 3GPP TR 38.901 [4] large scale model parameters

Parameter	3GPP Indoor-Office (InH)		3GPP Indoor-Factory (InF)	
	LOS	NLOS	LOS	NLOS
K-factor				
μ_K	7	N/A	7	N/A
σ_K	4	N/A	8	N/A
Delay Spread $\mathrm{lgDS} = \log_{10}(\mathrm{DS}/1\mathrm{s})$				
μ_{lgDS}	$-0.01\log_{10}(1+f_c)-7.69$	$-0.28\log_{10}(1+f_c)-7.17$	$\log_{10}(26(^{\mathrm{V}}/_{\mathrm{S}})+14)-9.35$	$\log_{10}(30(^{\mathrm{V}}/_{\mathrm{S}})+32)-9.44$
σ_{lgDS}	0.18	$0.10\log_{10}(1+f_c)+0.06$	0.15	0.19
Angle Spread of Arrival $\mathrm{lgASA} = \log_{10}(\mathrm{ASA}/1^\circ)$				
μ_{lgASA}	$-0.19\log_{10}(1+f_c)+1.78$	$-0.11\log_{10}(1+f_c)+1.86$	$-0.18\log_{10}(1+f_c)+1.78$	1.72
σ_{lgASA}	$0.12\log_{10}(1+f_c)+0.12$	$0.12\log_{10}(1+f_c)+0.06$	$0.12\log_{10}(1+f_c)+0.2$	0.3
Parameter Cross-Correlations				
ASA vs DS	0.8	0	0	0
ASA vs SF	-0.5	-0.4	0	0
ASA vs K	0	N/A	0	N/A
DS vs SF	-0.8	-0.5	0	0
DS vs K	-0.5	N/A	-0.7	N/A
SF vs K	0.5	N/A	0	N/A

In NLOS condition, the path loss is modeled using a two-slope approach that is defined as $\max(PL_{\mathrm{LOS}}, PL'_{\mathrm{NLOS}})$. In both models, $d_{3\mathrm{D}}$ is the 3D-distance between TX and RX in meter, and f_c is the carrier frequency in GHz. The InH model is valid for distances from 1 m to 150 m, and the InF model from 1 m to 600 m.

Furthermore, TR 38.901 defines large-scale model parameters that are for the most part frequency dependent. In Table 3, the large-scale model parameters applicable to the parameters evaluated in this paper are listed. For the InH scenario, both DS and ASA are frequency dependent. However, in the InF scenario, the DS model is not dependent on frequency, but on the ratio between room volume and surface area $^{\mathrm{V}}/_{\mathrm{S}}$. In the present scenario, this ratio equals $^{\mathrm{V}}/_{\mathrm{S}} = 1.59$. Lastly, the TR also defines frequency-independent parameter cross-correlations, which are also listed in Table 3. It should be noted, however, that the all-zero cross-correlation in the InF scenario – with the exception of DS vs K – probably is not a well-modeled representation of the propagation environment, but stems from a lack of underlying data. Secondly, the model is only validated for the frequency range from 0.1 GHz to 100 GHz. For lack of another model, the given parameters will still be used for comparison in the following sections.

5. Evaluation and Results

The output of the channel sounder system consists of a set of 1000 channel impulse response (CIR) snapshots corresponding to each of the VUCA antenna elements. The CIR snapshots are obtained by correlating the raw measurement data with a pre-recorded back-to-back calibration that includes all cabling and active components of the channel sounder setup. In order to suppress side lobes in time domain and for amplitude normalization, the estimated CIR snapshots for all frequencies are windowed in the frequency domain using a normalized Kaiser-Bessel window function with parameter $\beta = 6$.

Average power delay profiles (APDPs) are derived by incoherently averaging the squares of the magnitudes of the CIR snapshots and are used as the basis for further evaluation of LSPs. The averaging leads to a greatly reduced variance in power and a much smoother gradient of the profiles. A peak search algorithm with a threshold of 20 dB with regards to the global maximum magnitude of the APDP is used to identify multipath components (MPCs) in the form of local maxima. This threshold is in line with the ITU-R recommendation P.1407-8 [24] and was chosen because all measurements at both frequencies show a high enough signal-to-noise ratio (SNR) to satisfy it. The evaluation threshold limits the length of the power delay profile (PDP) and prevents noise from affecting the subsequent parameter estimation. It therefore has to be chosen well above the noise floor, but should at the same time be as large as possible. Investigations in [25] have shown that the relative estimation error introduced by the evaluation threshold is 11 % for 20 dB, 5.4 % for 25 dB and 2.4 % for 30 dB. To keep the estimation error consistent, a single evaluation threshold was applied to all measurements, although some supported a higher threshold. Evaluation of the dynamic range, defined as the distance between the maximum magnitude of the APDP and noise floor, shows that in NLOS, only 60 % of the measurements at 160 GHz would support a threshold of 25 dB, or 18 % for 30 dB. All measurements supported a threshold of 20 dB.

Based on the identified MPCs, the PL, K-factor, and RMS DS are evaluated. Furthermore, real-valued beamspace MUSIC (RB-MUSIC) [26] is used as direction of arrival (DoA) estimator to extract specular information from the CIR snapshots, enabling evaluation of the RMS ASA. The VUCA signal model and RB-MUSIC method is introduced in detail in [21].

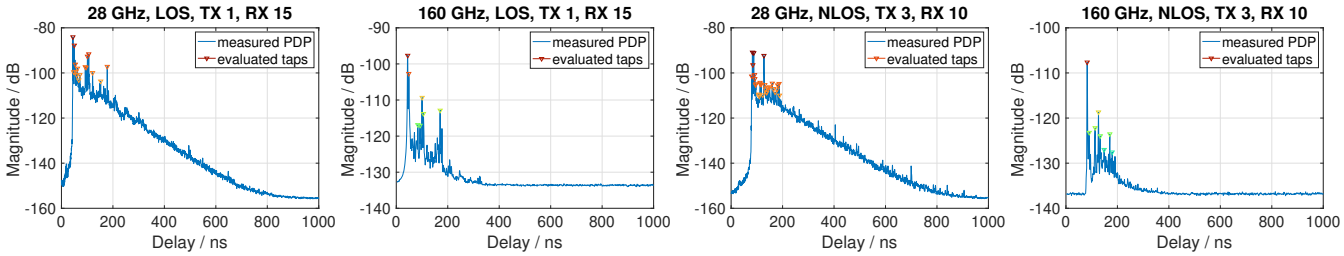

(a) Power delay profiles

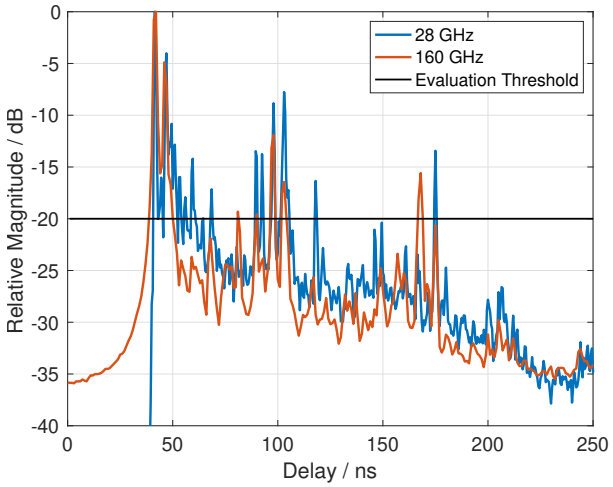

(b) LOS, TX position 1, RX position 15, 3D-distance 12.6 m

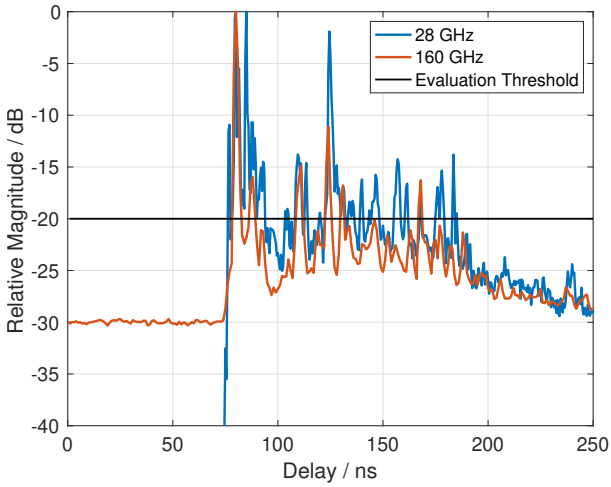

(c) NLOS, TX position 3, RX position 10, 3D-distance 22.8 m

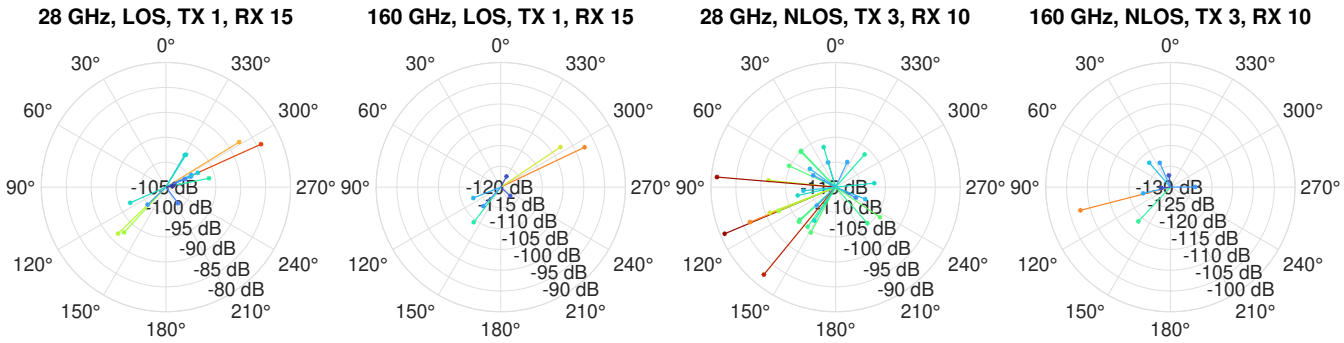

(d) Power angular profiles

Figure 5: Power delay and angular profiles at both frequencies.

In the following, the PL, K-factor, number of MPC, and RMS DS and ASA are evaluated. Frequency-dependent model parameters for PL, K-factor, and RMS DS and ASA are estimated and compared to the 3GPP TR 38.901 channel model in InH and InF scenarios. Lastly, cross-correlations between the large-scale model parameters are calculated and are also used to evaluate the similarity between the two frequencies.

5.1. Power Delay and Angular Profiles

In order to evaluate the results of the channel sounding campaign, APDPs are first derived based on the captured CIR snapshots. In Fig. 5a, several representative APDPs are shown, together with the identified MPCs. From left to right, the profiles correspond to the measurements taken in LOS with the TX at position 1 and the RX at position 15 at 28 GHz and 160 GHz, and in NLOS with the TX at position 3 and the RX at position 10. At both frequencies and in both conditions, specular MPCs are identified with delays of up to 200 ns, corresponding to path lengths of up to 60 m. Especially at 28 GHz, further dense or diffuse multipath components (DMCs) can be seen until the APDP falls below the noise floor with a magnitude of −155 dB. The noise floor at 160 GHz has a magnitude of −132 dB which can be explained by the −23 dB lower output power. Any DMC as exhibited at the lower frequency is hidden by this higher noise floor.

To further compare the measurements at the two frequencies, APDPs normalized to their respective maximum magnitude are shown in Figs. 5b and 5c in LOS and NLOS, together with the 20 dB evaluation threshold. In LOS, the direct component between TX and RX was received with a delay of 42 ns. An additional strong MPC was received 5 ns later at both frequencies. In the following 100 ns, several other distinct components can

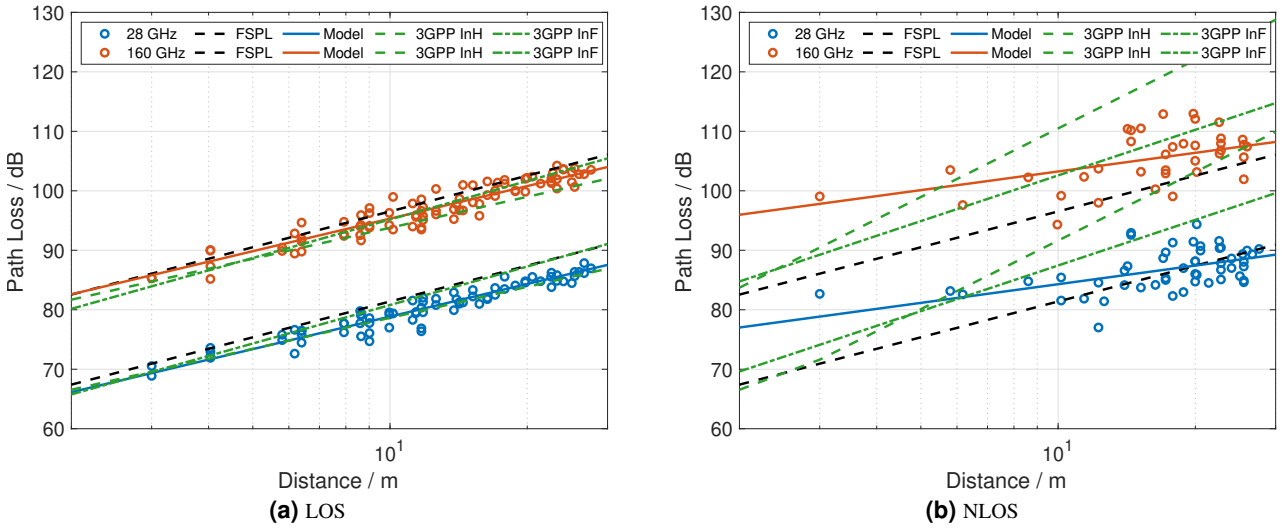

(a) LOS **(b)** NLOS

Figure 6: Path loss in LOS and NLOS conditions, with estimated and 3GPP models.

be seen at 28 GHz, but not at the higher frequency. Two MPCs with a delay of around 100 ns were received at both frequencies with a much higher relative magnitude at 160 GHz compared to 28 GHz. The last strong components were received with delays of approximately 170 ns until the APDP falls below the noise floor. While not all MPCs were received at both frequencies, the APDPs follow a similar trend and share most of the stronger components.

In NLOS, as displayed in Fig. 5c, the strongest component at both frequencies was received with a delay of 80 ns. At 28 GHz, a component with the same magnitude was received 5 ns later, which cannot be seen at 160 GHz. This could be due to a scatterer whose reflectivity differs markedly between the two frequencies – for example, because of surface roughness – or from an object present only during the 28 GHz measurements. Both APDPs share a similar trend, with the magnitude of the MPCs at 28 GHz are generally higher compared to 160 GHz, where most of the components fall below the evaluation threshold of 20 dB.

Specular information is shown in Fig. 5d in the form of power angular profiles (PAPs) in the same order and for the same positions as the APDPs in Fig. 5a. In LOS, the main component was evaluated to be impinging from 295 ° at both frequencies, with another strong component from approximately 302 °. Other distinct components were received from 110 ° to 140 ° at both 28 GHz and 160 GHz. Several components from 280 ° and 330 °, and from the same direction as the LOS path were only received at 28 GHz. Overall, the PAPs in LOS display a high degree of similarity, matching the results in [9]. In NLOS, the strongest component was impinging the RX from approximately 110 ° at both frequencies and a second distinct component can be seen from 140 °, with a much lower magnitude at 160 GHz however. Another strong component was received from 85 ° at 160 GHz that cannot be seen at the other frequency. The PAPs in NLOS show less similarity compared to LOS, which can be explained by the higher number of MPC that fall below the evaluation threshold at 160 GHz.

5.2. Path Loss

By summing up the magnitudes of the identified MPCs within the APDPs, the path loss was estimated for each MP. In Fig. 6, the evaluated PL is shown separately in LOS (Fig. 6a) and NLOS (Fig. 6b) condition for both frequencies. The measured values are indicated with circles in blue at 28 GHz and orange at 160 GHz, and the estimated models are plotted in solid lines of the same color. The free space path loss (FSPL) is also given as a dashed black line. Furthermore, both 3GPP models are also included in the figures: The InH model is plotted as a dashed green line, and the InF model as dash-dotted green line. In LOS, the path loss is slightly lower, but very close to FSPL at both frequencies for the entire measured distance. In NLOS, the path loss is 12 dB higher than FSPL for the minimum distance of 3 m, but gets close to it or even lower at 28 GHz for distances greater than 20 m. A frequency-dependent ABG PL model [27] according to (4) was parameterized using least squares fitting. and is plotted in Fig. 6 as solid lines. It is valid for distances ranging from 3 m to 27.6 m.

$$PL_{\mathrm{ABG}}(f,d) = 10\alpha \log_{10}(d) + \beta + 10\gamma \log_{10}(f) + \chi_{\sigma}^{\mathrm{ABG}}, \tag{4}$$

where α and γ show the dependence of path loss on 3D TX-RX distance d in meters and frequency f in GHz, and β is an optimized offset value for path loss in dB. $\chi_{\sigma}^{\mathrm{ABG}}$ is the lognormal random shadowing variable with corresponding standard deviation σ. Based on the measurement results, the model was evaluated to be

$$PL_{\mathrm{LOS}}(f,d) = 18.2 \log_{10}(d) + 29.2 + 21.7 \log_{10}(f), \tag{5a}$$
$$PL_{\mathrm{NLOS}}(f,d) = 10.4 \log_{10}(d) + 37.6 + 25.0 \log_{10}(f), \tag{5b}$$

with $\sigma_{\mathrm{LOS}} = 1.42$ and $\sigma_{\mathrm{NLOS}} = 3.43$.

Comparison with the 3GPP models reveals that in LOS at 28 GHz, the InH model is a great fit to the measured PL, which is in line with the results in [9]. The InF model slightly overestimates the PL, with values even higher than FSPL for distances greater than 25 m. At 160 GHz – where the model was not validated – both scenarios are still quite close to the measured data. The InH model values are close to underestimating the PL, whereas the InF model produces slightly higher values, between the estimated model in this paper and FSPL. In NLOS, neither of the 3GPP models is a good fit to the measured data in this scenario, again matching [9]. While the measured PL starts high for short distances and grows closer to FSPL for larger distances, both 3GPP models estimated a PL close to FSPL for short distances with much higher values for larger distances. Between both possible scenarios, the InF model is more in line with the measured data, but still not a good fit.

Table 4: Estimated large scale parameters

Parameter	LOS		NLOS	
	28 GHz	160 GHz	28 GHz	160 GHz
Number of evaluated MPCs				
Mean	12.5	7.09	25.5	13.9
Median	13	6	25	14
Std. Dev. σ	4.59	3.09	11.0	4.60
95% Quant.	20.5	12.3	42.9	19.7
K-factor in dB				
Mean	0.89	4.56	N/A	N/A
Median	0.41	3.76	N/A	N/A
Std. Dev. σ	3.64	4.16	N/A	N/A
95% Quant.	7.21	12.8	N/A	N/A
Delay Spread (DS) in ns				
Mean	16.3	16.5	28.2	28.4
Median	15.5	16.3	27.0	29.7
Std. Dev. σ	6.34	7.49	11.2	9.63
95% Quant.	26.2	28.6	45.8	45.3
Angle Spread of Arrival (ASA) in °				
Mean (°)	35.2	35.7	58.9	62.9
Median (°)	32.6	33.9	54.7	64.4
Std. Dev. σ	16.4	20.6	27.9	26.2
95% Quant.	26.2	28.6	45.8	45.3

5.3. Number of MPC and K-Factor

Analysis of the number of evaluated MPCs as given in Table 4 shows that at both frequencies, on average twice as many components were identified in NLOS compared to LOS. At the same time, the mean number of MPC at 28 GHz is generally almost double the number at 160 GHz. This observation is supported by the APDPs as displayed in Figs. 5b and 5c. It was concluded earlier that, while the general trend of the APDPs at the two frequencies is similar, the profiles at 28 GHz feature more distinct MPCs and that many of the components at 160 GHz fall below the evaluation threshold. Another possible explanation that MPC arriving closely together in delay domain are hidden at 160 GHz due to the lower measurement bandwidth is not proven true by examination of the APDPs.

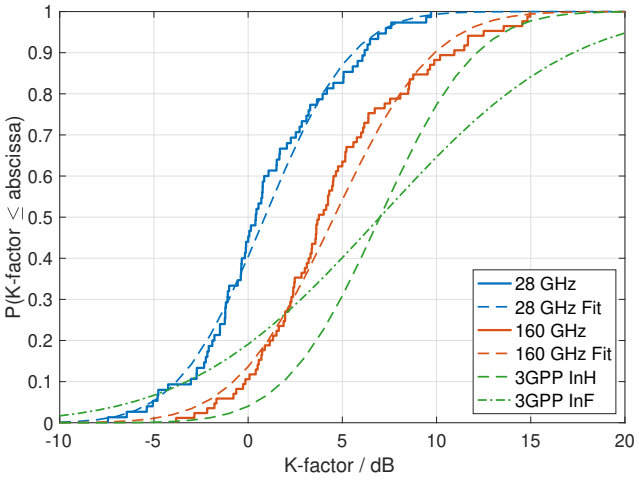

Figure 7: CDF of K-factor. Fitted and 3GPP models plotted in dashed lines.

In addition to the total number of MPC, the K-factor, or ratio between LOS component and all other components in LOS condition according to the 3GPP definition (6) was evaluated.

$$K = P_{\mathrm{LOS}} - 10\log_{10}\left(\sum_{n=1}^{N} 10^{P_n/10}\right), \tag{6}$$

where P_{LOS} is the power of the LOS component, N is the number of further components with a power of P_n. Table 4 lists the statistical parameters mean, median, standard deviation σ and 95%-quantile of the K-factor. Additionally, the cumulative density function (CDF) is shown in Fig. 7. At 28 GHz, the mean K-factor is evaluated as 0.89 dB, at 160 GHz it is 4.56 dB. In other words, at 28 GHz, the power of the LOS component is just slightly higher than the combined power of the remaining components. At 160 GHz, the ratio is higher, which means that there is more power in the LOS component compared to the rest. This is consistent with the higher absolute number of evaluated MPCs at 28 GHz compared to 160 GHz. A frequency-dependent model for the K-factor was estimated through linear regression and is given in Table 5 and displayed by dashed lines in Fig. 7. Additionally, the figure also displays the 3GPP models as dashed (InH) and dash-dotted (InF) green lines. It is directly apparent that neither model is a good fit to the measurement results, as they share a frequency-independent mean value of 7 dB with different standard deviations. In the presented scenario, much more power was received in the non-LOS components as compared to the data underlying the 3GPP models.

5.4. RMS Delay Spread

In addition to power metrics, the CIR snapshots were also evaluated in terms of delay and angular characteristics. The RMS DS was calculated based on the identified MPC, and the CDF is shown in Fig. 8. In LOS, the mean DS is 16.3 ns at 28 GHz, and 16.5 ns at 160 GHz, as indicated in Table 4. Similarly, in NLOS,

the mean DS is evaluated to be 28.2 ns and 28.4 ns for the two frequencies. Even though the number of evaluated MPC differs significantly between 28 GHz and 160 GHz, the mean DS does not appear to be frequency-dependent, which can also be seen in the model parameters listed in Table 5, but is in contrast to [9], where the DS was found to decrease with frequency.

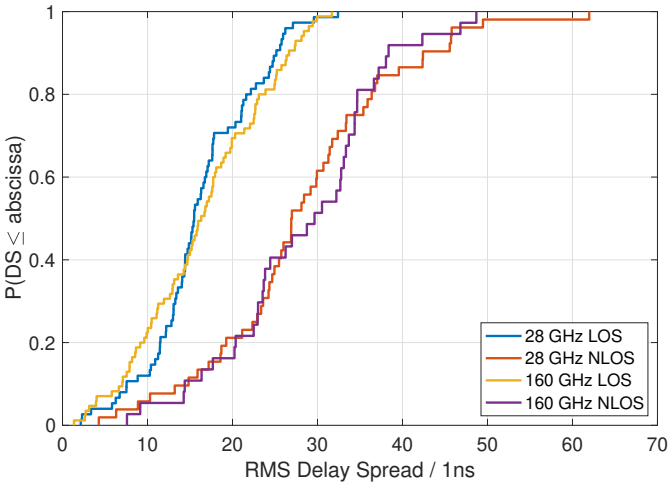

Figure 8: CDF of RMS DS.

For better comparison with the 3GPP models, the CDF is plotted on a logarithmic scale in Figs. 11a and 11b. Besides the CDF of the RMS DS, Figs. 11a and 11b also show the estimated log-normal fittings and 3GPP model parameters. The measurement data is plotted in blue at 28 GHz and in orange at 160 GHz, and the estimated fittings in dashed lines of the same color. The 3GPP models are plotted as dash-dotted lines: Green for InH at 28 GHz, blue at 160 GHz, and red for the InF model. Comparison between the 3GPP models, the estimated model and the measurement data shows that the InH model is similarly frequency-independent as the measured results, but that neither of the 3GPP models is a good fit in LOS. All three overestimate the DS, with the InF model producing the highest values. In NLOS, the measurement results and most models lie very close together, with the exception of the 3GPP InH model at 160 GHz that greatly under-estimates the DS.

To further characterize the DS, its dependency on the distance between TX and RX was evaluated as shown in Fig. 9. In LOS, an increase in DS with distance can be seen for both frequencies. A linear fit through the evaluated DS values shows a positive slope of 0.53 ns/m at 28 GHz, and 0.43 ns/m at 160 GHz. In NLOS, the distance dependency is less pronounced. At 28 GHz, the DS is nearly independent of distance with a change of 0.09 ns/m, and at 160 GHz the DS even gets slightly lower with growing distance with a slope of −0.19 ns/m.

5.5. RMS Angular Spread of Arrival

The angular characteristics of the channels were evaluated by analyzing the RMS ASA in a way similar to the RMS DS. The mean ASA was evaluated to be 35.2 ° at 28 GHz and 35.7 ° at 160 GHz in LOS, and 58.9 ° and 62.9 ° in NLOS. The CDF of the RMS ASA is displayed in Fig. 10. Table 4 also lists

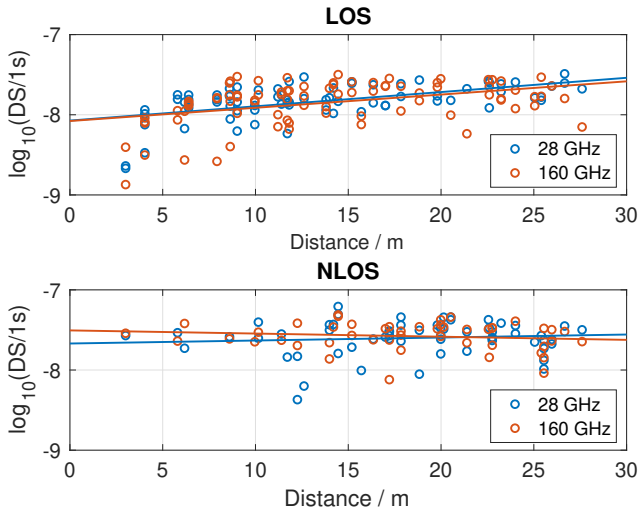

Figure 9: Distance dependency of RMS DS.

the median, standard deviation and 95%-quantile. The RMS ASA appears to be almost frequency independent, similar to the DS, as can also be seen in the model parameters given in Table 5. While the authors in [9] evaluated the azimuth spread of departure (ASD) which is not directly comparable to the ASA, a similar frequency independence was found.

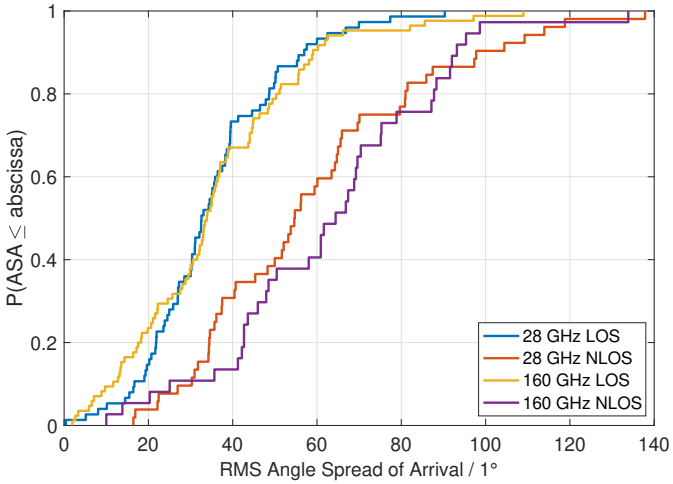

Figure 10: CDF of RMS ASA.

Figs. 11c and 11d show the CDF of the RMS ASA on logarithmic scale in LOS and NLOS. As previously, the measurement results at 28 GHz are plotted in a solid blue line, and those at 160 GHz in orange. Estimated model parameters are displayed in dashed lines of the same color. The 3GPP InH model is shown as dash-dotted lines in green at 28 GHz and in light blue at 160 GHz. Finally, the 3GPP InF model is plotted as dash-dotted lines in red at 28 GHz, and in dark blue at 160 GHz. In LOS, both 3GPP models are a good fit at 28 GHz, with the InH model fitting slightly better. Both 3GPP models underestimate the ASA at 160 GHz. In NLOS, the same observation can be made. The frequency independent InF model is a good fit, as is the InH model at 28 GHz, while it underestimates the ASA at 160 GHz.

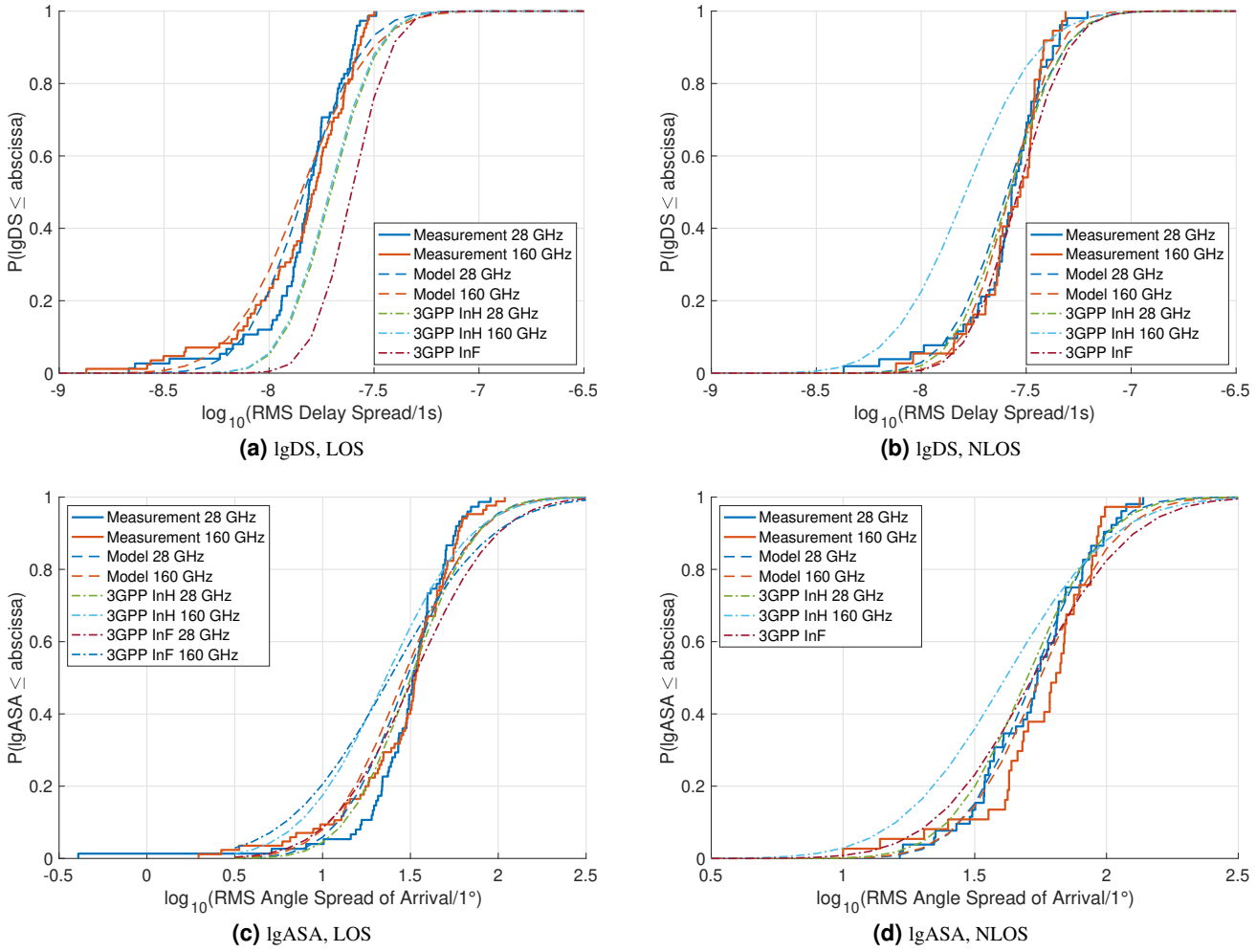

(a) lgDS, LOS **(b)** lgDS, NLOS

(c) lgASA, LOS **(d)** lgASA, NLOS

Figure 11: CDFs of RMS DS and ASA in LOS and NLOS conditions, with estimated and 3GPP model parameters.

Similar to the DS, the ASA was evaluated for distance dependency. Fig. 12 shows the ASA measurement results over distance for LOS (top) and NLOS (bottom) as circles, and the linear fit as solid lines. In LOS, the ASA has a positive slope of 0.87 °/m at 28 GHz, and 0.71 °/m at 160 GHz. In NLOS, the ASA seems to be almost independent of the distance at 28 GHz, with a slope of the linear fit of −0.18 °/m. At 160 GHz, the ASA decreases by −1.1 °/m. Comparison between the distance dependency of RMS DS and ASA reveals a high level of similarity between the two parameters.

5.6. Parameter Cross-Correlation

The parameter cross-correlations between estimated LSPs were calculated using the Pearson product-moment correlation coefficient [28] in logarithmic domain. Table 4 lists the correlations between ASA, DS, shadow fading (SF) and K-factor, both separately for each frequency and combined. The correlation coefficient can only have values between −1 and 1.

In general, the strongest correlation was evaluated to be between ASA and DS, with an overall coefficient of 0.62 in LOS and a slightly lower 0.48 in NLOS. No frequency dependence can be identified for the correlation between these

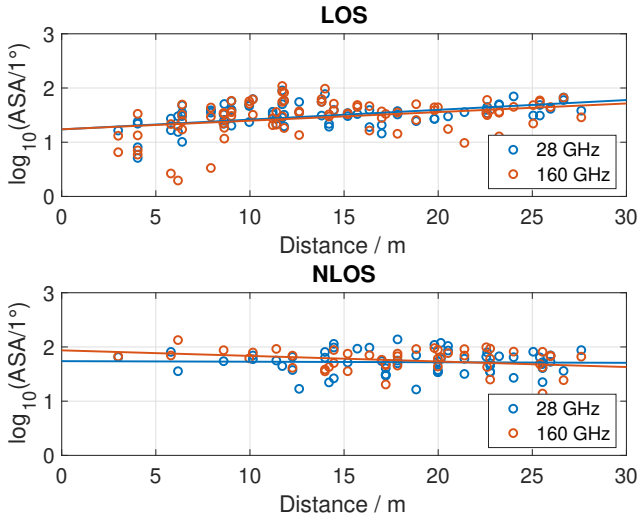

Figure 12: Distance dependency of RMS ASA.

Table 5: Estimated model parameters, f_c = 28 GHz & 160 GHz

Parameter	LOS	NLOS
K-factor		
Mean μ_K	$4.94\log_{10}(1+f_c/1\text{GHz})-6.33$	N/A
Std. Deviation σ_K	$0.69\log_{10}(1+f_c/1\text{GHz})+2.63$	N/A
Delay Spread $\text{lgDS}=\log_{10}(\text{DS}/1\text{s})$		
Mean μ_{lgDS}	$-0.02\log_{10}(1+f_c/1\text{GHz})-7.80$	$0.02\log_{10}(1+f_c/1\text{GHz})-7.62$
Std. Deviation σ_{lgDS}	$0.06\log_{10}(1+f_c/1\text{GHz})+0.13$	$-0.05\log_{10}(1+f_c/1\text{GHz})+0.29$
Angle Spread of Arrival $\text{lgASA}=\log_{10}(\text{ASA}/1^\circ)$		
Mean μ_{lgASA}	$-0.03\log_{10}(1+f_c/1\text{GHz})+1.52$	$0.04\log_{10}(1+f_c/1\text{GHz})+1.67$
Std. Deviation σ_{lgASA}	$0.03\log_{10}(1+f_c/1\text{GHz})+0.27$	$0.03\log_{10}(1+f_c/1\text{GHz})+0.17$

Table 6: Parameter cross-correlations

Parameter	LOS			NLOS		
	28 GHz	160 GHz	Comb.	28 GHz	160 GHz	Comb.
ASA vs DS	0.63	0.61	0.62	0.49	0.48	0.48
ASA vs SF	−0.06	−0.01	−0.04	0.49	0.20	0.32
ASA vs K	−0.47	−0.60	−0.50	N/A	N/A	N/A
DS vs SF	0.36	0.39	0.37	0.77	0.48	0.61
DS vs K	−0.26	−0.34	−0.29	N/A	N/A	N/A
SF vs K	0.15	0.39	0.23	N/A	N/A	N/A

LSPs. Another positive correlation can be seen between DS and SF, with a coefficient of 0.37 in LOS, and 0.77 at 28 GHz and 0.48 at 160 GHz in NLOS. The ASA is evaluated not to be correlated with the SF in LOS, however in NLOS, both a correlation and frequency dependence was identified. At 28 GHz, the correlation coefficient was evaluated to be 0.49, and 0.20 at 160 GHz. Both ASA and DS are negatively correlated with the K-factor, with a slightly larger coefficient at 160 GHz for both parameters. SF and K-factor are only lightly correlated with a slightly higher coefficient at 160 GHz.

Comparison with the parameter cross-correlation values listed in 3GPP TR 38.901 reveals that neither model fits the measurement results well. While the InH model also shows a strong correlation between ASA and DS in LOS and both ASA and DS are also negatively correlated with the K-factor, the coefficients of the 3GPP model generally are higher than values presented in this paper. The InF model with almost all zero coefficients clearly is incomplete and also does not match the measurement results.

Table 7: Frequency cross-correlations

Parameter	LOS	NLOS	Combined
ASA	0.58	0.31	0.60
DS	0.61	0.31	0.63
K	0.41	N/A	N/A
SF	0.46	0.56	0.52

In an attempt to quantize the similarity between the radio channels at 28 GHz and 160 GHz, the cross-correlation coefficients for the various LSPs at both frequencies were also calculated. Table 7 lists the correlation coefficients for LOS and NLOS, and for both conditions combined. The results show a positive correlation between the frequencies for all parameters, with the strongest correlation for ASA and DS in LOS, and for SF in NLOS. Based on this observation, the channels indeed are correlated, which is also supported by the similarity of the APDPs and PAPs as presented earlier in Fig. 5. The results also show a higher correlation of the channels in LOS than in NLOS.

6. Conclusion

This paper presented channel measurements in an industrial-style open office scenario at 28 and 160 GHz. The receiver was placed at 45 measurement positions for each of the three transmitter positions, resulting in 135 measurements for each frequency. Of all measurement positions, 85 were in LOS, and 50 in NLOS condition, and the results were evaluated in terms of power metrics and delay and angular characteristics, and compared to relevant 3GPP channel model parameters.

In terms of power metrics, frequency-dependent models for path loss and K-factor were estimated, and the number of identified multipath components (MPCs) was examined. Comparison of the path loss to the 3GPP TR 38.901 channel model reveals that, in LOS condition, the InF model slightly over-estimates the PL, but that the InH model is a good fit, especially at 28 GHz. In NLOS condition, neither model is a good fit, but the InF model is closer to the measurement results and the fitted model. The K-factor at 28 GHz was found to be 0.89 dB. At 160 GHz, more power was found in the LOS component compared to the rest with a K-factor of 4.56 dB. At both frequencies, the 3GPP model value of 7 dB is not a good fit.

The average number of MPC at 28 GHz was found to be twice as high as at 160 GHz. At the same time, the mean RMS DS and ASA show almost no frequency dependency in this scenario, which becomes apparent both in the CDF plots, and in the estimated model parameters. The 3GPP models for DS and ASA are also almost frequency independent. In LOS condition, neither DS model is a good fit for the measurement results, how-

ever in NLOS, both InH and InF models align to the measured data at 28 GHz. The 3GPP models for the ASA are both a good fit at 28 GHz, but underestimate at 160 GHz. However, it should be noted that the model was only validated for frequencies up to 100 GHz Some similarities to a similar study published in [9] were found. In both studies, the PAP shapes were found to follow a common trend at both frequencies, and the 3GPP TR 38.901 PL model in LOS condition matches well to the measurements. Although little to no frequency dependence of the AS was found in both studies, the actual values of DS and AS do not align well.

RMS DS and ASA were furthermore evaluated for their distance dependency. It was found that both parameters increase with distance in LOS condition at both frequencies. In NLOS, the parameters are almost distance independent at 28 GHz and slightly decrease with distance at 160 GHz

Finally, large scale parameter cross-correlations were calculated. Both DS and ASA are negatively correlated with the K-factor, with a slightly larger coefficient at 160 GHz. A strong correlation without frequency dependency was found between DS and ASA. SF is correlated with varying degree to the other LSPs. Comparison with the 3GPP InH model did not reveal a good fit with the 3GPP values generally being higher. The parameter cross-correlation was also used in an attempt to evaluate the similarity between the channels at the two frequencies. Results show a positive correlation for all parameters with the strongest ones between ASA and DS, and a generally higher correlation in LOS than in NLOS.

Acknowledgment

The authors acknowledge the financial support by the Federal Ministry of Education and Research of Germany in the program of ”Souverän. Digital. Vernetzt.” Joint project 6G-RIC, project identification number: 16KISK020K, and joint project 6G-LICRIS, project identification number: 16KISK141.

References

[1] *World Radiocommunication Conference 2023 (WRC-23) – Provisional Final Acts*, International Telecommunication Union (ITU) Std., Dec. 2023.

[2] *TeraHertz technology (THz); Identification of frequency bands of interest for THz communication systems*, European Telecommunications Standards Institute (ETSI) Group Report, March 2024.

[3] *3GPP TS 38.101-2 – User Equipment (UE) radio transmission and reception; Part 2: Range 2 Standalone (version 15.26.0 Release 15)*, European Telecommunications Standards Institute (ETSI) Technical Specification, Aug. 2024.

[4] 3GPP, “Study on channel model for frequencies from 0.5 to 100 GHz,” 3GPP, Technical Report (TR) 38.901, 2020, version 16.1.0.

[5] M. Schmieder, A. Schultze, N. Kullig, R. Askar, M. Peter, and W. Keusgen, “Angle-resolved channel measurements at 28 and 160 GHz in open office industrial-like environment,” in *2025 19th European Conference on Antennas and Propagation (EuCAP)*, 2025, pp. 1–5.

[6] S. Ju and T. S. Rappaport, “142 GHz multipath propagation measurements and path loss channel modeling in factory buildings,” in *ICC 2023 - IEEE International Conference on Communications*, 2023, pp. 5048–5053.

[7] S. Ju, D. Shakya, H. Poddar, Y. Xing, O. Kanhere, and T. S. Rappaport, “142 GHz sub-terahertz radio propagation measurements and channel characterization in factory buildings,” *IEEE Transactions on Wireless Communications*, vol. 23, no. 7, pp. 7127–7143, 2024.

[8] Y. Wang, C. Wang, X. Liao, Y. Chen, Z. Yu, and G. Wang, “Millimeter wave and sub-THz channel measurements, models and comparisons in indoor industrial environment,” in *2024 IEEE 99th Vehicular Technology Conference (VTC2024-Spring)*, 2024, pp. 1–5.

[9] M. F. De Guzman and K. Haneda, “Comparison of indoor propagation channels at 28 GHz and 140 GHz bands,” in *2024 18th European Conference on Antennas and Propagation (EuCAP)*. IEEE, 2024, pp. 1–5.

[10] X. Liao, L. Fan, Y. Wang, Z. Yu, G. Wang, Y. Chen, and J. Zhang, “Measurement-based channel characterization in indoor IIoT scenarios at 220 GHz,” in *2024 IEEE Wireless Communications and Networking Conference (WCNC)*, 2024, pp. 1–6.

[11] C. E. Reinhardt, V. V. Elesina, J. M. Eckhardt, T. Doeker, L. C. Ribeiro, and T. Kürner, “Channel measurements in an industrial environment for access point-to-sensor communication at 300 GHz,” in *2024 15th German Microwave Conference (GeMiC)*, 2024, pp. 308–311.

[12] A. Schultze, M. Schmieder, S. Wittig, H. Klessig, M. Peter, and W. Keusgen, “Angle-resolved THz channel measurements at 300 GHz in an industrial environment,” in *2022 IEEE 95th Vehicular Technology Conference: (VTC2022-Spring)*, 2022, pp. 1–7.

[13] A. Schultze, M. Schmieder, R. Askar, M. Peter, W. Keusgen, and T. Eichler, “Dual-polarized sub-THz channel measurements in D-band in an industrial environment,” in *2024 Joint European Conference on Networks and Communications & 6G Summit (EuCNC/6G Summit)*, 2024, pp. 582–586.

[14] D. Dupleich, A. Ebert, Y. Völker-Schöneberg, L. Löser, M. Boban, and R. Thomä, “Spatial/temporal characterization of propagation and blockage from measurements at sub-THz in industrial machines,” in *2023 17th European Conference on Antennas and Propagation (EuCAP)*, 2023, pp. 1–5.

[15] J. M. Eckhardt, A. Schultze, R. Askar, T. Doeker, M. Peter, W. Keusgen, and T. Kürner, “Uniform analysis of multipath components from various scenarios with time-domain channel sounding at 300GHz,” *IEEE Open Journal of Antennas and Propagation*, vol. 4, pp. 446–460, 2023.

[16] J. E. Galeote-Cazorla, G. Martínez-García, A. Ramírez-Arroyo, A. V. Alejos, and J. F. Valenzuela-Valdés, “Spatial

characterization of indoor radio channel in the D-Band at 165 GHz," in *2025 19th European Conference on Antennas and Propagation (EuCAP)*, 2025, pp. 1–5.

[17] R. Takahashi, A. Ghosh, M. Mao, and M. Kim, "Channel modeling and characterization of access, d2d, and backhaul links in a corridor environment at 300 ghz," *IEEE Transactions on Antennas and Propagation*, vol. 73, no. 4, pp. 1954–1968, 2025.

[18] M. Kim, A. Ghosh, R. Takahashi, and K. Shibata, "Indoor channel measurement at 300 GHz and comparison of signal propagation with 60 GHz," *IEEE Access*, vol. 11, pp. 124 040–124 054, 2023.

[19] A. Schultze, M. Schmieder, R. Askar, M. Peter, W. Keusgen, and T. Eichler, "Comparison of sub-THz radio channel characteristics at 158 GHz and 300 GHz in a shopping mall scenario," in *2024 18th European Conference on Antennas and Propagation (EuCAP)*, 2024, pp. 1–5.

[20] A. Al-jzari, J. Hu, and S. Salous, "Millimeter-wave and sub-THz channel measurements and characterization analysis in a street canyon scenario," in *2024 18th European Conference on Antennas and Propagation (EuCAP)*, 2024, pp. 1–5.

[21] H.-A. Nguyen, W. Keusgen, and T. Eichler, "Instantaneous direction of arrival measurements in mobile radio channels using virtual circular array antennas," in *2016 IEEE Globecom Workshops (GC Wkshps)*. IEEE, 2016, pp. 1–7.

[22] S. Saad, J. Davies, and O. Davies, "Analysis and design of a circular TE01 mode transducer," *IEE Journal on Microwaves, Optics and Acoustics*, vol. 1, no. 2, pp. 58–62, 1977.

[23] M. Friese, "Multitone signals with low crest factor," *IEEE Transactions on Communications*, vol. 45, no. 10, pp. 1338–1344, 1997.

[24] *Multipath propagation and parameterization of its characteristics*, International Telecommunication Union Recommendation ITU-R P.1407-8, 2021.

[25] M. Peter, "Measurement, characterization and modeling of millimeter-wave channels : from 60 GHz to 5G," Doctoral Thesis, Technische Universität Berlin, Berlin, 2017. [Online]. Available: http://dx.doi.org/10.14279/depositonce-6541

[26] C. P. Mathews and M. D. Zoltowski, "Eigenstructure techniques for 2-D angle estimation with uniform circular arrays," *IEEE Transactions on signal processing*, vol. 42, no. 9, pp. 2395–2407, 1994.

[27] S. Sun, T. S. Rappaport, S. Rangan, T. A. Thomas, A. Ghosh, I. Z. Kovacs, I. Rodriguez, O. Koymen, A. Partyka, and J. Jarvelainen, "Propagation path loss models for 5G urban micro-and macro-cellular scenarios," in *2016 IEEE 83rd Vehicular Technology Conference (VTC Spring)*. IEEE, 2016, pp. 1–6.

[28] J. Lee Rodgers and W. A. Nicewander, "Thirteen ways to look at the correlation coefficient," *The American Statistician*, vol. 42, no. 1, pp. 59–66, 1988.